HHS Public Access

Author manuscript

Acta Biomater. Author manuscript; available in PMC 2020 May 01.

Published in final edited form as:

Acta Biomater. 2019 May ; 90: 37–48. doi:10.1016/j.actbio.2019.03.041.

Fabrication and Mechanical Characterization of 3D Printed Vertical Uniform and Gradient Scaffolds for Bone and Osteochondral Tissue Engineering

Sean M. Bittner[a,b,c], **Brandon T. Smith**[a,b,c,d], **Luis Diaz-Gomez**[a,b,c], **Carrigan D. Hudgins**[a,b,c], **Anthony J. Melchiorri**[a,b,c], **David W. Scott**[e], **John P. Fisher**[c,f], **Antonios G. Mikos**[a,b,c,*]

[a]Department of Bioengineering, Rice University, 6500 Main Street, Houston, TX 77030, USA;

[b]Biomaterials Lab, Rice University, 6500 Main Street, Houston, TX 77030, USA;

[c]NIH / NIBIB Center for Engineering Complex Tissues, USA;

[d]Medical Scientist Training Program, Baylor College of Medicine, Houston, TX, USA;

[e]Department of Statistics, Rice University, 6100 Main Street, Houston, TX 77030, USA;

[f]Fischell Department of Bioengineering, University of Maryland, College Park, MD, USA.

Abstract

Recent developments in 3D printing (3DP) research have led to a variety of scaffold designs and techniques for osteochondral tissue engineering; however, the simultaneous incorporation of multiple types of gradients within the same construct remains a challenge. Herein, we describe the fabrication and mechanical characterization of porous poly(ε-caprolactone) (PCL) and PCL-hydroxyapatite (HA) scaffolds with incorporated vertical porosity and ceramic content gradients *via* a multimaterial extrusion 3DP system. Scaffolds of 0 wt% HA (PCL), 15 wt% HA (HA15), or 30 wt% HA (HA30) were fabricated with uniform composition and porosity (using 0.2 mm, 0.5 mm, or 0.9 mm on-center fiber spacing), uniform composition and gradient porosity, and gradient composition (PCL-HA15-HA30) and porosity. Micro-CT imaging and porosity analysis demonstrated the ability to incorporate both vertical porosity and pore size gradients and a ceramic gradient, which collectively recapitulate gradients found in native osteochondral tissues. Uniaxial compression testing demonstrated an inverse relationship between porosity, ϕ, and compressive modulus, E, and yield stress, σ_y, for uniform porosity scaffolds, however, no differences were

*To whom correspondence may be addressed: Antonios G. Mikos, PhD, Department of Bioengineering, MS-142, BioScience Research Collaborative, Rice University, 6500 Main Street, Houston, TX-77030, mikos@rice.edu, Tel: (713) 348-5355, Fax: (713) 348-4244.

Disclosure Statement

No competing financial interests exist.

This manuscript describes the fabrication and mechanical characterization of “dual” porosity/ceramic content gradient scaffolds produced *via* a multimaterial extrusion 3D printing system for osteochondral tissue engineering. Such scaffolds are designed to better address the simultaneous gradients in architecture and mineralization found in native osteochondral tissue. The results of this study demonstrate that this technique may serve as a template for future advances in 3D printing technology that may better address the inherent complexity in such heterogeneous tissues.

observed as a result of ceramic incorporation. All scaffolds demonstrated compressive moduli within the appropriate range for trabecular bone, with average moduli between 86±14 – 220±26 MPa. Uniform porosity and pore size scaffolds for all ceramic levels had compressive moduli between 205±37 – 220±26 MPa, 112±13 – 118±23 MPa, and 86±14 – 97±8 MPa respectively for porosities ranging between 14±4 – 20±6%, 36±3 – 43±4%, and 54±2 – 57±2%, with the moduli and yield stresses of low porosity scaffolds being significantly greater ($p<0.05$) than those of all other groups. Single (porosity) gradient and dual (composition/porosity) gradient scaffolds demonstrated compressive properties similar ($p > 0.05$) to those of the highest porosity uniform scaffolds (porosity gradient scaffolds 98±23 – 107±6 MPa, and 102±7 MPa for dual composition/porosity gradient scaffolds), indicating that these properties are more heavily influenced by the weakest section of the gradient. The compression data for uniform scaffolds were also readily modeled, yielding scaling laws of the form $E \sim (1-\phi)^{1.27}$ and $\sigma_y \sim (1-\phi)^{1.37}$, which demonstrated that the compressive properties evaluated in this study were well-aligned with expectations from previous literature and were readily modeled with good fidelity independent of polymer scaffold geometry and ceramic content. All uniform scaffolds were similarly deformed and recovered despite different porosities, while the large-pore sections of porosity gradient scaffolds were significantly more deformed than all other groups, indicating that porosity may not be an independent factor in determining strain recovery. Moving forward, the technique described here will serve as the template for more complex multimaterial constructs with bioactive cues that better match native tissue physiology and promote tissue regeneration.

Keywords

3D Printing; gradient; porous scaffold; tissue engineering

1. Introduction

Nearly one-fifth of adults in the U.S. suffer from cartilage and osteochondral unit-related injuries and pathologies.[1] These conditions collectively represent the most common cause of disability in individuals over 30 and disproportionately affect high-impact athletes and other load-bearing professions. Osteochondral lesions are notably complex due to the intricated structure of the tissue and are usually associated with great instability, pain, and impaired function. A variety of clinical techniques have been used to treat these injuries, including autologous chondrocyte implantation, microfracture, autograft, and mosaicplasty.[2–10] These methods have several limitations, including graft deterioration/lack of integration, mechanically-insufficient cartilage formation, and donor site morbidity, leading to often insufficient patient outcomes.[11–13]

The complexity of the osteochondral unit requires a well-organized scaffold with designed physical and biochemical gradients in order to facilitate new tissue growth. Native cartilage is avascular and has a low cell density of chondrocytes, leading to a limited capacity for self-renewal compared to other tissues. Articular cartilage and subchondral bone tissues have extremely heterogeneous gradient structures and a number of different biological cues; an inability to fabricate constructs matching this level of complexity has prevented the progress of restorative solutions.[14–17] In particular, designing a tissue engineered scaffold for the

cartilage-bone interface requires an accurate recreation of load-bearing and stress distribution, spatiotemporal action of biochemical factors, and graded porous architecture. Interconnected, open porosity is essential to facilitate cell migration, nutrient flow, and vascular network formation.[18–22] Of particular importance from a materials perspective is the requirement to match the mechanical properties of the native tissue. Importantly, osteochondral tissues present a very organized structure with different degrees of mineralization and pore sizes which must be mimicked accurately.[20,23,24] An inability to fabricate biomimetic constructs with adequate mechanical and biological properties using the traditional tissue engineering strategies has prevented further progress of engineered solutions.[25,26] Certain techniques, such as gas foaming, solvent casting, or freeze-drying, have often led to the development of scaffolds with some combination of an uncontrolled/random porous structure, insufficient mechanical properties, and a lack of control over varying compositions throughout the construct.[27–30]

Extrusion printing, a type of additive manufacturing (AM) is an attractive vehicle for the fabrication of complex tissue engineering scaffolds of clinically-relevant size, as constructs produced are in most cases limited only by the template computer-aided design (CAD) model, the achievable fiber resolution (based on the needle diameter and rheological properties of the solution), and the number of different material dispensers.[31–33] Many extrusion printers offer the ability to print multiple materials with independent printing instructions, easily creating composite structures. Extrusion 3DP is particularly useful for heterogeneous tissue scaffolds, such as proposed here for the osteochondral unit, due to the ease of co-printing materials and the control of the material deposition layer-by-layer.[33–45] Furthermore, it is possible to incorporate architectural and compositional gradients to mimic native tissue organization with high precision and reproducibility.[46]

Common polymeric materials for 3DP bone scaffolds include poly(ε-caprolactone) (PCL) and poly(D,L-lactic-co-glycolic acid) (PLGA).[47] These materials have widely demonstrated biocompatibility, impart strong base mechanical properties required for hard tissues, and allow for easy reproduction of printed scaffolds.[35,48–54] Ceramic materials, such as hydroxyapatite (HA), have also been widely studied for bone tissue engineering applications due to their good mechanical strength and similarity to the mineralized areas phase of native bone tissue.[31,32,55–61] They can be used as an additive material to impart varying mechanical properties or mineralized layers in heterogeneous tissues, and their osteoconductive properties make them particularly beneficial for engineering of bone and bone-interface tissues such as the osteochondral unit.[62] Several studies have demonstrated the important effect of ceramic particle morphology on the osteointegration, osteoinduction, and osteoconduction. It has been reported that HA particle size plays an important role on the rate of resorption and the ability of the material to promote bone growth.[63–65] Furthermore, the size of the HA particles also plays a crucial role in the degradation rate of the scaffolds. Microsized HA particles are usually reported to lead to a marked decrease in the resorbability of the scaffolds since fragmentation of the particles to submicron sizes is needed before they can be processed by the cells also resulting in the relocation of the HA that could affect the preset concentration in gradient scaffolds.[65] On the other hand, nanosized HA incorporated in polymeric scaffolds are easily degraded by osteoclasts, macrophages and even osteoblasts, and can be directly used by osteoblasts to form new bone

tissue in situ.[64,66] Additive Manufacturing, in particular, has improved the ability of researchers to pattern ceramics, yielding constructs with discrete and continuous gradients.[67] Previous studies from this laboratory and others have shown that the mechanical properties of composite scaffolds can be altered through changing the internal pore morphology and the materials printed, allowing researchers employing extrusion printing to precisely tune the scaffold strength, yield, and other properties to meet a specific need.[43,45,62,68,69] Tissue engineering scaffolds that address biochemical or architectural gradients individually are therefore not sufficiently complex to recapitulate the desired properties of these tissues. Additionally, evaluations of how the mechanical properties of such gradient scaffolds compare to those of traditional uniform constructs remain underexplored, particularly an examination of how strains are distributed within these matrices.

In the present work, porous poly(ε-caprolactone)-based scaffolds were fabricated via multimaterial 3DP with vertical gradients in porosity and ceramic content to mimic the variations in composition and pore morphology in the native osteochondral unit. Printing reproducibility and scaffold structures were assessed for inclusion in the study. The printed constructs were then subjected to uniaxial mechanical compression to evaluate the relationship between scaffold porosity, ceramic content, and compressive modulus and yield stress. Specifically, the scope of this study focused on the following considerations: 1) Demonstrating the feasibility of incorporating both porosity and dual composition/porosity gradients within 3DP polymeric scaffolds; 2) Identifying a relationship between design criteria (ceramic content, porosity) and measured mechanical properties (compressive modulus, yield stress) for uniform scaffolds; 3) Investigation of the effects of porosity gradient incorporation on the compressive properties of scaffolds; and 4) Investigation of the compressive properties of dual composition/porosity gradient scaffolds, which are designed to mimic the osteochondral anatomy. Additionally, changes in porosity and strain after scaffold recovery were evaluated.

2. Materials and Methods

2.1. Scaffold printing

Hydroxyapatite (HA, average particle size 208 nm, Sigma-Aldrich, St. Louis, MO) was homogeneously mixed with polycaprolactone (PCL, nominal molecular weight 50,000 Da, Polysciences, Warrington, PA, Lot no. 25090) in different proportions (Table 1) using a mortar and pestle. PCL molecular weight was determined before and after printing using an Acquity Advanced Polymer Chromatography system (Waters, Milford, MA), as described previously.[60] Extrusion printing of materials was similarly carried out as described in a previous study.[60] Briefly, the powdered mixtures were placed in metal cartridges, heated to 160°C, and extruded through a 22G blunt tip needle (0.4 mm inner diameter) using a commercial 3D printing system (3D Bioplotter; EnvisionTEC, Gladbeck, Germany). To create computer models for printing, rectangular scaffolds with an aspect ratio of 2 following ASTM D695 (6 mm width and length, 12 mm height) were designed in SketchUp (Trimble, Sunnyvale, CA) and sliced into 37 layers (0.32 mm slicing thickness) using BioplotterRP Software (EnvisionTEC, Gladbeck, Germany).[70] Three separate filling

patterns (designated as small-, medium-, or large-pore designs) were created by drawing parallel straight strands with 0.7, 1.0, or 1.4 mm on-center spacing, and the fiber orientation of each new layer was perpendicular to the previous layer, leading to the formation of square pores with 0.2 (small-pore), 0.5 (medium-pore), or 0.9 mm (large-pore) fiber spacing in each direction (Figure 1). Uniform scaffolds were printed from a single rectangular model while porosity gradient scaffolds were printed as three stacked models with the same 0.32 mm layer separation as for uniform scaffolds. Dual (porosity, material) gradient scaffolds were printed similarly to porosity gradient scaffolds, with the additional step of switching the material for each stacked model corresponding to a different section of the scaffold (bottom: PCL-HA30/0.9 mm spacing; middle: PCL-HA15/0.5 mm spacing; top: PCL/0.2 mm spacing). In total, thirteen groups were developed, as shown in Table 1. Printing conditions (pressure, speed, pre- and post-flow, wait time) were set for each composition using values from an earlier preliminary study and are shown in Table 2.

2.2. Printing validation and physical characterization of 3D scaffolds

The structure and HA distribution of the scaffolds (n=65 scaffolds total) were analyzed *via* microcomputed tomography (micro-CT), using a SkyScan 1272 X-ray Micro-CT (Bruker, Kontich, Belgium). Images were obtained by at 12 μm/pixel resolution with Al 0.25 mm filter at voltage and current settings of 60 kV and 166 mA, respectively. Scans were reconstructed, resliced, and analyzed using NRecon and CTAn software (Bruker, Billerica, MA) as well as LabView (National Instruments, Austin, TX). For structural analysis, all scaffolds were subjected to a ± 10% quality control window on fiber diameter with a nominal value of 500 μm; printed scaffolds with fiber sizes outside of this range were rejected for inclusion in the study and were reprinted with the same conditions. For porosity analyses, the scanned object volumes were converted in binary images using a threshold of 25–255 for PCL and 50–255 for PCL-ceramic. A proportional volume of interest of 85% scale of each of the x, y, and z axes equally spaced from the scaffold edges was selected to analyze the porosity and interconnectivity of each sample both before and after compression. For estimated values of fiber spacing (used in Figure S2), values were calculated by measuring the spacing between two sets of adjacent fibers at 5 different slices of the scaffold (n=10/scaffold). For strain evaluation, the height of the entire scaffold for uniform porosity scaffolds and that of each discrete section within gradient porosity scaffolds was measured before compression and again after compression and recovery.

2.3. Mechanical properties evaluation

The compressive moduli and yield stresses of all uniform and gradient scaffolds (n=5/group) were measured in a mechanical testing bench (858 MiniBionixII®, MTS, Eden Prairie, MN; 10 kN load cell, ± 1 N sensitivity) and calculated using the TestStar 790.90 mechanical data analysis package included in the manufacturer's software. Scaffolds were compressed perpendicularly to the printing plane at a crosshead speed of 1 mm/min after an initial pre-load of 25 N up to 20% strain. Stress-strain curves were calculated from the load vs. displacement data using the initial external dimensions of each sample. After compression, scaffolds were allowed to recover over a period of 24–48 hours before being scanned again *via* micro-CT using the conditions described above. The compressive modulus was estimated using the slope of the linear portion of the stress-strain curve. Yield stress was

estimated by a 0.2% offset to the stress-strain curve. The changes in porosity, $\Delta\phi$, were calculated as shown in Equation 1:

$$\Delta\phi = \phi_2 - \phi_1 \quad (1)$$

where ϕ_1 and ϕ_2 are the pre- and post-compression porosities respectively.

Given the vast amount of literature on the relationship between compressive properties and construct porosity for synthetic polymers, it was also of interest to attempt to model the compressive moduli and yield stresses as continuous functions of porosity. According to Gibson *et al.*, the compressive properties of porous polymeric scaffolds can be modeled using Equations 2 and 3:

$$E \sim (1 - \phi)^n \quad (2)$$

$$\sigma_y \sim (1 - \phi)^m \quad (3)$$

where E is the compressive modulus, σ_y is the yield stress, ϕ is the internal porosity, and n and m describe the model architecture.[71,72] The values of n and m for most polymers have been suggested previously to be within the range of (1,2).[71–75] In order to generate models for the relationships between porosity and modulus/yield stress in this experiment, the compressive moduli and yield stresses of uniform scaffolds (0.2 mm, 0.5 mm, 0.9 mm) from all three material groups (PCL, HA15, HA30) were plotted against their pre-compression porosities on a log-log scale.

In strain distribution evaluation, final strains ε_f following compression and subsequent recovery were calculated using the basic strain formula shown in Equation 4:

$$\varepsilon_f(\%) = \frac{\Delta\text{height}}{height_{initial}} * 100 \quad (4)$$

where Δheight is the change in height before compression and after recovery, and $height_{initial}$ is the initial height of the scaffold before compression.

2.4. Statistical analysis

Statistics were analyzed using Graphpad Prism (Graphpad Software, La Jolla, CA). All results were expressed as mean values with standard deviations. One-way analysis of variance (ANOVA) and Tukey's multiple comparison post-test were used. Differences were considered significant for $p<0.05$.

3. Results

3.1. Printing validation and pre-compression characterization

PCL and PCL-HA composite scaffolds were fabricated *via* multimaterial extrusion 3DP as described in Section 2.1 For uniform material, uniform porosity scaffolds of PCL, HA15, or HA30 (Table 1), the object was assigned a single material and porosity and printed layer-by-layer (Figure 1a,b). For uniform material, gradient porosity scaffolds, one material was assigned to the object along with each of the three (0.7, 1.0, and 1.4 mm) nominal spacing designs and printed layer-by-layer (Figure 1c). For dual gradient (gradient composition, gradient porosity) scaffolds, each of the three sections of the scaffold was assigned both a unique material and a unique filling pattern (Figure 1d). Each section of these scaffolds was printed layer-by-layer before the print cartridge was exchanged to begin printing the next section. In total, 13 groups were evaluated, as shown in Table 1. Printing conditions (pressure, speed, pre- and post-flow, wait time) were determined for each composition and are shown in Table 2. Using these conditions, a nominal fiber diameter of 0.5 mm was selected, with corresponding nominal fiber spacings of 0.2, 0.5, and 0.9 mm for the small-pore, medium-pore, and large-pore patterns as described above. The structure of all scaffolds (n=65) were analyzed *via* micro-CT as described in Section 2.2. Figure 2 depicts micro-CT reconstructions of each of the scaffold groups used (a–c: a top-down view of PCL/small-pore, HA15/medium-pore, HA30/large-pore scaffolds; d–f: side view of these scaffolds; g–j: side view of PCL, HA15, HA30 single gradient scaffolds and dual gradient scaffold). The group average and sample-specific fiber sizes for each scaffold are included in Supplemental Data (Figure S1, Figure S2, Table S1).

After validating the printing methodology, the porosity of each scaffold was determined using 3D reconstructions of each *via* micro-CT and associated software. Micro-CT reconstructions of each type of scaffold are shown in Figure 2. For porosity measurements, a proportional volume of interest of 85% scale of each of the x, y, and z-axes was used, which allowed for the inclusion of all internal porosity while excluding artifacts at the edge of each scaffold. Gradient scaffolds were evaluated similarly, with the porosity of each section individually determined for later evaluation of strain distribution, and comparison of the pre-compression porosities of all scaffolds/gradient sections demonstrated statistical similarity ($p>0.05$) between all Small/Gradient Small, Medium/Gradient Medium, and Large/Gradient Large scaffolds/sections respectively. These pre-compression porosities were later used to model the compressive properties of uniform scaffolds. In general, scaffold porosity was well defined, with >90% interconnected pores. Pre-compression porosities for all scaffolds are shown in Table S2.

3.2. Uniaxial compression of scaffolds and determination of compressive properties

Scaffolds were subjected to uniaxial compression as described in Section 2.3. The compressive modulus and yield stress for each scaffold were then determined from the stress-strain curve. As shown in Figures 3 and 4, small-pore (0.2 mm) scaffolds (porosity range 14±4 – 20±6%) had significantly higher values of compressive modulus (207±36 MPa, 220±26 MPa, 205±37 MPa for PCL, HA15, HA30 respectively) and yield stress (12±2 MPa, 11±3 MPa, 12±3 MPa for PCL, HA15, HA30 respectively) compared to all other

scaffold groups ($p<0.05$). Medium-pore (0.5 mm) and large-pore (0.9 mm) scaffolds (porosity ranges 36±3 – 43±4% and 54±2 – 57±2%) did not show a significant difference in compressive modulus (Medium: 117±19 MPa, 118±23 MPa, 112±13 MPa, Large: 86±14 MPa, 97±7 MPa, 97±8 MPa for PCL, HA15, HA30 respectively) or yield stress (Medium: 7±1 MPa, 7±2 MPa, 6±1 MPa, Large: 5±1 MPa, 5±1 MPa, 5±1 MPa for PCL, HA15, HA30 respectively) based on these statistical analyses, however, analysis on a continuous basis was also conducted as shown. Both porosity and dual gradient scaffolds showed statistically similar compressive moduli (98±23 MPa, 102±8 MPa, 107±6, 102±7 MPa for PCL, HA15, HA30, Dual gradient respectively) and yield stresses (5±1 MPa, 5±1 MPa, 5±1, 6±1 MPa for PCL, HA15, HA30, Dual gradient respectively) to the medium and large pore uniform scaffolds.

It was also of interest to identify a continuous relationship between scaffold porosity and resulting compressive properties (modulus, yield stress). The compressive modulus and yield stress of each uniform porosity (0.2 mm, 0.5 mm, 0.9 mm) scaffold from each composition (PCL, HA15, HA30) was plotted against its pre-compression porosity on a log-log scale as shown in Figures 5 and 6, and linear regression was applied to determine model equations for each relationship. For the compressive modulus and yield stress respectively, these model equations were determined to be $\log(E) = 1.27\log(1-\phi) + 2.39$ and $\log(\sigma_y) = 1.37\log(1-\phi) + 1.15$. These data are displayed on absolute scales in Figures S3 and S4.

3.3. Evaluation of morphology changes and strain distribution

The effects of the initial scaffold porosity on the change in architecture after compression and recovery were also examined. Figure 7 depicts a representative dual gradient scaffold before and after compression. After compressive testing and recovery, scaffolds were scanned and reconstructed to determine the effect of compression on the porosity of the scaffolds. All pre-compression and post-recovery porosities for each scaffold are found in Supplemental Data (Table S2 and Figure S5), and a comparison of the changes in porosity changes is shown in Figure S6. For these measurements, each small-pore, medium-pore, and large-pore section of the gradient scaffolds were evaluated separately for individual strains and porosity changes. There were no statistical differences ($p>0.05$) observed between changes in porosity across all scaffolds.

Regarding the strain after recovery of the scaffolds, the heights of uniform scaffolds and each section of gradient scaffolds were measured by micro-CT before compression and after recovery, and the final strain was calculated using Eq. 2 in Section 2.3. These results are shown in Figure S7a, organized by pore group. The final strain after recovery for each scaffold was independent of ceramic concentration; within each uniform pore design, PCL, HA15, and HA30 scaffolds had statistically similar final strains (between 7±1 and 9±2%, 8±1 and 10±1%, and 7±1 and 10±1% respectively for Small, Medium, Large pore scaffolds respectively) after recovery, indicating that the incorporated ceramic did not significantly impact the compressive behavior of the construct. Additionally, dual gradient scaffolds demonstrated no statistical differences with porosity gradient scaffolds overall nor within each section, indicating that the incorporation of a ceramic content gradient does not impact the recovery behavior. Furthermore, the large pore design section of the gradient scaffolds

had significantly higher strains (between 19±8 and 22±3%) than all other groups. Scaffolds with the same composition had statistically similar strains independent of pore size. Figure S7b shows strain analysis data plotted on a continuous basis rather than grouped. The strains of large pore gradient sections are consistently higher than those of uniform counterparts, while there is no observable trend among the other groups. Finally, comparison of uniform pore scaffolds with their gradient section counterparts led to several observations. As stated previously, the large pore section of the gradient scaffolds had significantly higher strains than the uniform large pore scaffolds. However, on comparison of the small-pore and medium-pore groups, in most cases, the strains of the uniform porosity scaffolds and those of their gradient section counterparts (e.g. small-pore vs. gradient small-pore) were not statistically different ($p>0.05$). One scaffold comparison was outside of this observation; specifically, the HA15 small-pore scaffold had a significantly higher strain than its gradient small-pore counterpart ($p<0.05$).

4. Discussion

In this work, PCL scaffolds were fabricated *via* multimaterial 3DP with vertical porosity and HA gradients, in order to develop a construct more closely matching the variations in architecture and composition found in the native osteochondral unit. Specifically, this study was focused on four key considerations, namely: 1) the feasibility of incorporating both porosity and dual composition/porosity gradients within 3DP polymeric scaffolds; 2) the relationship between scaffold design variations (ceramic content, porosity) and measured compressive properties (compressive modulus, yield stress) for uniform scaffolds; 3) the effects of incorporating a porosity gradient on these properties; and 4) the compressive properties of dual composition/porosity gradient scaffolds, which are designed to mimic the osteochondral anatomy better. Additionally, changes in porosity and strain after scaffold recovery were evaluated.

Scaffolds were printed according to the conditions listed in Table 2, with a nominal desired fiber diameter of 0.5 mm ± 0.05 mm, and were then scanned using micro-CT to determine the actual fiber diameter and pre-compression porosity. As demonstrated in Figure S1, scaffolds were consistently printed with reasonable fidelity to the original design, indicative of the reliability of extrusion printing as has been widely demonstrated in recent years.[31–33,76] After porosity and fiber size measurements were completed, all scaffolds were subjected to uniaxial compression as described above. As shown in Figures 3 and 4, on a grouped basis, small-pore (0.2 mm) scaffolds had significantly higher compressive moduli and yield stresses than all other groups ($p<0.05$), while medium-pore (0.5 mm) and large-pore (0.9 mm) scaffolds did not demonstrate a significant difference in compressive modulus and yield stress. In general, these data are consistent with previously established trends between compressive properties and porosity; despite not being statistically different, the medium-pore (0.5 mm) scaffolds tended to have higher compressive moduli than large-pore (0.9 mm) scaffolds.[71] The discrepancy in the lack of a statistical difference can be attributed to the much higher values for small-pore scaffolds relative to those of the medium-pore and large-pore scaffold groups, which may mask statistical differences between the latter two groups. As demonstrated above, this discrepancy is addressed when considering the scaffolds on a continuous basis. The primary desired result in grouping scaffolds by

designed pore size was the investigation of single and dual gradient behavior, which is not readily modeled on a continuous basis due to the varying porosity. Single (porosity) gradient scaffolds showed statistically similar compressive properties to medium-pore and large-pore uniform scaffolds, indicating that the overall compressive properties of the gradient structure are influenced more by those sections with higher porosities (and therefore reduced compressive properties) rather than being best modeled as a number average.

Considering prior literature, the compressive modulus and yield stress are highly dependent on scaffold geometry. The compressive moduli for Large pore, pure PCL scaffolds (56±4% pre-compression porosity) were 86±14 MPa in this study. Lee *et al.* found compressive moduli for 1:1 PCL:PLGA scaffolds using a similar cross-hatch pattern, aspect ratio, and porosity (57%) to be on the order of 120 MPa.[77] Shor *et al.* observed compressive moduli of 59 MPa and 30 MPa for PCL scaffolds with the same cross-hatch pattern, an aspect ratio of 1 (20mm diameter, 20mm height), and 60% and 70% porosity respectively, as well as 84 MPa and 76 MPa for 25 wt% HA scaffolds of the same architectures.[78] Conversely, for solid injection molded PCL scaffolds (50mm width and length, 4mm height), Ragaert *et al.* found compressive moduli on the order of 455 MPa.[79] Heo *et al.* used a similar printing process to develop 40 wt% HA/PCL scaffolds with an aspect ratio of 0.5 (10mm width/length, 5mm height) and ~72% internal porosity, and observed compressive moduli on the order of 3 MPa.[80] Huang *et al.* did not report experimental porosities from their study, however their fabrication of PCL and 10 wt% and 20 wt% HA scaffolds using the same cross-hatch pattern and an aspect ratio of 1.25 (4mm width/length, 5mm height) led to compressive moduli of 48, ~60, and 75 MPa respectively.[81] Finally, Kim *et al.* observed compressive moduli of 30.1 MPa and 24.2 MPa for 10 wt% HA and PCL scaffolds with 66.7% porosity, 0.4 aspect ratio (5mm width/length, 2mm height) and the same cross-hatch pattern.[82]

The compressive moduli and yield stresses were statistically similar independent of ceramic content within the same pore size group (0.2 mm, 0.5 mm, 0.9 mm). Additionally, the dual gradient scaffold group demonstrated compressive moduli and yield stresses statistically similar to those of the other gradient scaffolds, indicating that the incorporation of a ceramic gradient also does not significantly affect the mechanical properties of the construct. The incorporation of ceramics within polymer matrices has been shown previously to increase the compressive and tensile strength of scaffolds.[30,78,80,81,83–85] However, the reinforcement mechanism by which this phenomenon occurs remains not well understood. In one example, it was reported that an increase in compressive modulus was observed for HA-incorporated scaffolds but not for other similar ceramics such as tricalcium phosphate (TCP).[86] Similarly, another experiment reported demonstrated a decrease in Young's modulus for 10 wt% HA scaffolds and an increase for 20 wt% and 30 wt% HA scaffolds compared to pure PCL scaffolds.[83] There may be several reasons for the lack of reinforcement observed, including the particle size and base compressive properties of the polymer. In terms of particle size, in this study nano-sized (~200 nm diameter) HA was used in 0, 15, and 30 wt% concentrations. Previous studies in the literature have used a variety of particle sizes, including nano and microscale particles, and compositions, including those used here as well as higher concentrations (40, 50 wt%).[30,78,80,81,83–85] Additionally, all scaffolds in this study had compressive moduli within the range of human trabecular

bone, and the incorporation of HA may not offer observable reinforcement to such constructs.[60,85,87] In a previous study, the compressive properties of multimaterial scaffolds printed as segmented fibers with different compositions were investigated using both HA and TCP, and, similarly, no statistical differences were observed between compressive moduli of PCL and PCL-ceramic composites (30 wt% HA, 30 wt% TCP, or 15 wt% HA/15 wt% TCP formulations) of a different geometry (10 mm diameter, 5 mm height cylindrical scaffolds).[60] Finally, the lack of compressive property reinforcement after HA incorporation may be due to a suboptimal interface between the particles and the polymer matrix, as it is known that the transfer of stress within particulate composites is highly dependent on the interface.[88] Previous attempts to improve the interface between the polymer matrix and the incorporated ceramic have often involved the use of solvents, such as tetrahydrofuran [85,89] or chloroform [80], which may present biocompatibility concerns.

Although it may be difficult to evaluate the ceramic/polymer interface beyond the characterization we have conducted thus far, the data obtained here suggest that there was no dominant effect (weakening or reinforcing) observed in this study. At a minimum, it has been demonstrated that the mechanical properties were not weakened by the introduction of sizeable aggregate failure points. Taken together, the results of this study and those found in prior literature indicate that a better understanding of the mechanism for ceramic reinforcement is needed.

As shown in Figures 5 and 6, model regression equations were determined for the continuous relationships between porosity and compressive modulus/yield stress in the form of the model by Gibson *et al.*, which demonstrates the relationship between the compressive properties and porosity of bulk polymeric scaffolds.[71,72] The values of n and m for compressive modulus and yield stress were 1.27 and 1.37 respectively, which are within the suggested range of (1,2); these results yielded scaling laws of the form $E \sim (1-\phi)^{1.27}$ and $\sigma_y \sim (1-\phi)^{1.37}$ respectively, suggesting a near-linear logarithmic relationship between these variables.[71,73–75] These data demonstrate that the compressive properties evaluated in this study align well with expectations from previous literature and are readily modeled with good fidelity independent of polymer scaffold geometry and ceramic content.

The change in scaffold porosity post-compression was determined for all scaffolds as described above. For porosity and strain analyses, each section of the gradient scaffolds was examined separately for porosity changes within each section. As hypothesized, uniaxial compression led to an overall decrease in porosity, as the vertical spacing between fibers was reduced. However, as demonstrated in Figure S6, there were no statistical differences ($p>0.05$) observed between changes in porosity across all scaffold groups before compression and after recovery. This result may indicate that the magnitude of deformation of the internal architecture is proportional to the scaffold's pre-compression porosity. Alternatively, the pre-compression porosity may not be an independent factor in determining morphological changes due to compression.

The final evaluation of this study was an investigation of the distribution of strain across the scaffolds, yielding information about the behavior of gradient scaffolds with variable mechanical properties. In order to build tissue engineering constructs that recapitulate the

properties of native tissues, an understanding of scaffold strain behavior under load is required, particularly for constantly strained musculoskeletal tissues such as the osteochondral unit. For strain distribution, the final strains following compression and recovery were determined for all uniform scaffolds as well as for all discrete sections within gradient scaffolds (Table 1). As shown in Figure S7a, the final strains of the overall gradient scaffolds were additionally considered (calculated using Eq. 2 for the overall change in the height of the entire gradient). As identified in the study objectives, three investigations were of interest when considering strain distribution: the effect of ceramic incorporation within the scaffold, the effect of scaffold porosity (pore design), and the effect of the gradient structure. The final strain of each scaffold was demonstrated to be independent of ceramic concentration, as PCL, HA15, and HA30 scaffolds of the same pore design had statistically similar final strains. As was observed in the compressive modulus and yield stress data, the incorporated ceramic did not impact the strain behavior of the construct to a noticeable amount, and similarly, dual gradient scaffolds showed no significant differences with single gradient scaffolds in all cases. As hypothesized, the large pore sections of gradient scaffolds had statistically higher strains than all other groups, which is in agreement with the modulus and yield stress data reported in this study, as deformation mainly occurs in the large pore section leading to similarities between the overall behavior of gradient scaffolds and higher porosity uniform scaffolds rather than those of lower porosities. The overall gradient scaffolds demonstrated statistically similar strain behavior to the uniform scaffolds, indicating that the small-pore and medium-pore sections of the gradient were much less vertically compressed as a result of the large-pore section bearing the load. Interestingly, all uniform scaffolds of the same composition had statistically similar strains independent of pore size, indicating that porosity may not be an independent factor in determining strain. The authors attribute this difference to the specific geometry of the scaffolds under load. As with all uniform porosity scaffolds used in this study, the large pore scaffold groups follow the aspect ratio of 2 as described in Methods. However, while the overall gradient scaffold adheres to this aspect ratio, each discrete section of the gradient does not. The large pore section of the gradient scaffold, therefore, has the same length and width as the corresponding large pore uniform scaffold, but only one-third the height of those scaffolds, resulting in a different recovery profile. These conclusions are supported by the additional comparison of final strains on a continuous basis as shown in Figure S7b, which shows the same data on a continuous basis to remove any loss of related information associated with grouping the scaffolds. The large pore sections of gradient scaffolds, which had the largest porosities, again demonstrated disproportionately high strains relative to all other groups, which displayed no apparent trend.

There remain several areas still to be investigated in the future. The osteochondral unit is extremely complex as described in the Introduction section, and the dual gradient scaffolds still provide a very simplified representation of the native osteochondral unit *in vivo*. In particular, the ceramic gradient has been represented as step-change sections of different concentrations rather than a continuous gradient, although previous studies in the literature have similarly approximated these gradients as step change sections.[48,60,90–94] Additionally, the method of extrusion printing used in this study fabricates constructs layer-by-layer, where each layer is deposited, and printing is paused before depositing the next

layer. This process necessarily creates a breakage in filament between layers. Although there remains a possibility that such printing can lead to the formation of failure points at the contacts between layers, micro-CT imaging demonstrates that there is a fusion between layers of all uniform and gradient scaffolds, and in our previous study, it was demonstrated that the fusion point of segmented fibers does not serve as a failure point.[60] Finally, in printing the single and dual gradient scaffolds, there was a necessary offset as designed in this study due to the pore sizes selected for each section. Future studies will address this offset by appropriately adjusting the pore size to fit the CAD design perfectly.

The compressive testing conducted in this study reflects the primary scope, which was to characterize the static material properties of single and dual gradient scaffolds. Additionally, in this study scaffolds were compressed and allowed to recover prior to post-compression scanning and characterization. The micro-CT and mechanical testing systems used are separate units, and scaffolds would have recovered during scanning if conducted immediately after compression leading to inaccurate characterization. It would instead be of great interest to investigate stress relaxation and creep recovery, which was not conducted in this study. Finally, all compression in this study was applied in the direction of the gradient axis. However, it may be valuable in the future to observe potential differences in the architecture/property relationships when applying compression perpendicularly or tangentially to the gradient plane as opposed to in line.

The pore geometry selected in this study was a 90° cross-hatch pattern, which allowed us to evaluate the compressive mechanical properties of the uniform and porosity and dual gradient scaffolds. However, particularly due to the native complexity of the osteochondral unit as noted, future investigation into the compressive properties of various pore geometries would make for an interesting parametric study, and a number of compressive property models have been previously developed for porous scaffolds with different pore geometries. Among others, studies by Moroni *et al.*[95], Lee *et al.*[77], Van Bael *et al.*[96], and Sobral *et al.*[21] investigated the static and dynamic mechanical properties, as well as cell seeding efficiency in the latter study, as a result of varying pore geometries. Similarly, Al-Ketan *et al.* investigated structure-property relationships for a variety of metallic scaffold pore geometries using a powder fusion printing technique and evaluated the ability of different mathematical models (such as the model considered here) to predict resulting mechanical properties accurately.[75]

Finally, as the focus of this study was on scaffold mechanical characterization, no *in vitro* experimentation was conducted. However, in the future, it would be interesting to evaluate the effects of both porosity and ceramic gradients on cell behavior. In particular, it will be relevant to explore differences in cell growth and morphology between areas of different ceramic concentrations. Future *in vitro* and later *in vivo* experiments will need to address these and other additional areas in order to adequately demonstrate the use of these scaffolds for osteochondral repair.

5. Conclusions

Recent developments in AM and 3DP research have led to the development of a variety of scaffold designs and techniques for osteochondral tissue engineering. New biofabrication techniques for incorporating vertical and horizontal gradients have been introduced; however, to date, these techniques are still largely limited to single gradients of either material or architecture, while constructs intended for complex tissue regeneration may require the simultaneous inclusion of multiple types of gradients together. In this study, porous PCL and PCL-HA scaffolds were fabricated *via* multimaterial 3DP with incorporated vertical gradients in porosity and ceramic content. Uniaxial compression testing demonstrated an inverse relationship between porosity and compressive modulus and yield stress; however, no differences were observed between scaffolds of different ceramic concentrations at similar porosities. Porosity gradient scaffolds demonstrated compressive properties similar to those of the highest porosity scaffolds, indicating that these properties are more heavily influenced by the weakest section of the gradient. Dual gradient scaffolds demonstrated both of these behaviors; the compressive modulus and yield stress were similar to large pore uniform and pore gradient scaffolds, and the incorporation of a ceramic gradient did not substantially impact these properties. When observing the strain behavior of the scaffolds, uniform-pore scaffolds had similar values of strain despite different initial porosities. By contrast, the large-pore sections of gradient scaffolds were statistically significantly more deformed than all other sections, indicating that the porosity of a scaffold may not be an independent factor in determining strain. As shown in the compressive property analyses, the addition of HA ceramic did not alter the strain behavior significantly. These experiments demonstrate that the fabricated scaffolds incorporate porosity changes similar to those found in the native osteochondral unit as well as compressive properties in the range of human trabecular bone.

Supplementary Material

Refer to Web version on PubMed Central for supplementary material.

Acknowledgements

We acknowledge support by the National Institutes of Health (P41 EB023833 and R01 AR068073) and the RegenMed Development Organization (2017-601-002) in the preparation of this work. S.M.B also acknowledges support from the National Science Foundation Graduate Research Fellowship Program. B.T.S received support from Ruth L. Kirschstein Fellowships from the National Institute of Dental and Craniofacial Research (F31 DE027586), B.T.S acknowledges the Baylor College of Medicine Medical Scientist Training Program. L.D-G acknowledges Consellería de Cultura, Educación e Ordenación Universitaria for a Postdoctoral Fellowship (Xunta de Galicia, ED481B 2017/063).

References

[1]. Helmick CG, Felson DT, Lawrence RC, Gabriel S, Hirsch R, Kwoh CK, Liang MH, Kremers HM, Mayes MD, Merkel PA, Pillemer SR, Reveille JD, Stone JH, National Arthritis Data Workgroup, Estimates of the prevalence of arthritis and other rheumatic conditions in the United States: Part I, Arthritis Rheum 58 (2008) 15–25. doi:10.1002/art.23177. [PubMed: 18163481]

[2]. Harris J, Brophy R, Siston R, Flanigan D, Treatment of Chondral Defects in the Athlete's Knee, Arthrosc. J. Arthrosc. Relat. Surg 26 (2010) 841–852.

[3]. Huey DJ, Hu JC, Athanasiou KA, Unlike Bone, Cartilage Regeneration Remains Elusive, Science 338 (2012) 917–921. doi:10.1126/science.1222454. [PubMed: 23161992]

[4]. Smith GD, Knutsen G, Richardson JB, A clinical review of cartilage repair techniques, J. Bone Joint Surg. Br 87-B (2005) 445–449. doi:10.1302/0301-620X.87B4.15971.

[5]. Marcacci M, Kon E, Delcogliano M, Filardo G, Busacca M, Zaffagnini S, Arthroscopic Autologous Osteochondral Grafting for Cartilage Defects of the Knee: Prospective Study Results at a Minimum 7-Year Follow-up, Am. J. Sports Med 35 (2007) 2014–2021. doi: 10.1177/0363546507305455. [PubMed: 17724094]

[6]. Salzmann GM, Sauerschnig M, Berninger MT, Kaltenhauser T, Schönfelder M, Vogt S, Wexel G, Tischer T, Sudkamp N, Niemeyer P, Imhoff AB, Schöttle PB, The dependence of autologous chondrocyte transplantation on varying cellular passage, yield and culture duration, Biomaterials 32 (2011) 5810–5818. doi:10.1016/j.biomaterials.2011.04.073. [PubMed: 21592563]

[7]. Filardo G, Vannini F, Marcacci M, Andriolo L, Ferruzzi A, Giannini S, Kon E, Matrix-Assisted Autologous Chondrocyte Transplantation for Cartilage Regeneration in Osteoarthritic Knees: Results and Failures at Midterm Follow-up, Am. J. Sports Med 41 (2013) 95–100. doi: 10.1177/0363546512463675. [PubMed: 23104612]

[8]. Eldracher M, Orth P, Cucchiarini M, Pape D, Madry H, Small Subchondral Drill Holes Improve Marrow Stimulation of Articular Cartilage Defects, Am. J. Sports Med 42 (2014) 2741–2750. doi:10.1177/0363546514547029. [PubMed: 25167994]

[9]. Gobbi A, Karnatzikos G, Kumar A, Long-term results after microfracture treatment for full-thickness knee chondral lesions in athletes, Knee Surg. Sports Traumatol. Arthrosc 22 (2014) 1986–1996. doi:10.1007/s00167-013-2676-8. [PubMed: 24051505]

[10]. Mosher TJ, MRI of Osteochondral Injuries of the Knee and Ankle in the Athlete, Clin. Sports Med 25 (2006) 843–866. doi:10.1016/j.csm.2006.06.005. [PubMed: 16962428]

[11]. Hangody L, Dobos J, Baló E, Pánics G, Hangody LR, Berkes I, Clinical Experiences With Autologous Osteochondral Mosaicplasty in an Athletic Population: A 17-Year Prospective Multicenter Study, Am. J. Sports Med 38 (2010) 1125–1133. doi:10.1177/0363546509360405. [PubMed: 20360608]

[12]. Temenoff JS, Mikos AG, Review: tissue engineering for regeneration of articular cartilage, Biomaterials 21 (2000) 431–440. doi:10.1016/S0142-9612(99)00213-6. [PubMed: 10674807]

[13]. Yang HS, La W-G, Bhang SH, Kim H-J, Im G-I, Lee H, Park J-H, Kim B-S, Hyaline Cartilage Regeneration by Combined Therapy of Microfracture and Long-Term Bone Morphogenetic Protein-2 Delivery, Tissue Eng. Part A 17 (2011) 1809–1818. doi:10.1089/ten.tea.2010.0540. [PubMed: 21366427]

[14]. Castro NJ, O'Brien J, Grace Zhang L, Integrating biologically inspired nanomaterials and table-top stereolithography for 3D printed biomimetic osteochondral scaffolds, Nanoscale 7 (2015) 14010–14022. doi:10.1039/C5NR03425F. [PubMed: 26234364]

[15]. Lam J, Lu S, Meretoja VV, Tabata Y, Mikos AG, Kasper FK, Generation of osteochondral tissue constructs with chondrogenically and osteogenically predifferentiated mesenchymal stem cells encapsulated in bilayered hydrogels, Acta Biomater 10 (2014) 1112–1123. doi:10.1016/j.actbio. 2013.11.020. [PubMed: 24300948]

[16]. Lee J-S, Hong JM, Jung JW, Shim J-H, Oh J-H, Cho D-W, 3D printing of composite tissue with complex shape applied to ear regeneration, Biofabrication 6 (2014) 024103. doi: 10.1088/1758-5082/6/2/024103. [PubMed: 24464765]

[17]. Lu S, Lam J, Trachtenberg JE, Lee EJ, Seyednejad H, van den Beucken JJJP, Tabata Y, Kasper FK, Scott DW, Wong ME, Jansen JA, Mikos AG, Technical Report: Correlation Between the Repair of Cartilage and Subchondral Bone in an Osteochondral Defect Using Bilayered, Biodegradable Hydrogel Composites, Tissue Eng. Part C Methods 21 (2015) 1216–1225. doi: 10.1089/ten.tec.2015.0117. [PubMed: 26177155]

[18]. Perez RA, Mestres G, Role of pore size and morphology in musculo-skeletal tissue regeneration, Mater. Sci. Eng. C 61 (2016) 922–939. doi:10.1016/j.msec.2015.12.087.

[19]. Chan BP, Leong KW, Scaffolding in tissue engineering: general approaches and tissue-specific considerations, Eur. Spine J 17 (2008) 467–479. doi:10.1007/s00586-008-0745-3. [PubMed: 19005702]

[20]. Karageorgiou V, Kaplan D, Porosity of 3D biomaterial scaffolds and osteogenesis, Biomaterials 26 (2005) 5474–5491. doi:10.1016/j.biomaterials.2005.02.002. [PubMed: 15860204]

[21]. Sobral JM, Caridade SG, Sousa RA, Mano JF, Reis RL, Three-dimensional plotted scaffolds with controlled pore size gradients: Effect of scaffold geometry on mechanical performance and cell seeding efficiency, Acta Biomater 7 (2011) 1009–1018. doi:10.1016/j.actbio.2010.11.003. [PubMed: 21056125]

[22]. Velasco MA, Narváez-Tovar CA, Garzón-Alvarado DA, Design, Materials, and Mechanobiology of Biodegradable Scaffolds for Bone Tissue Engineering, BioMed Res. Int (2015). doi: 10.1155/2015/729076.

[23]. Roohani-Esfahani S-I, Newman P, Zreiqat H, Design and Fabrication of 3D printed Scaffolds with a Mechanical Strength Comparable to Cortical Bone to Repair Large Bone Defects, Sci. Rep 6 (2016) 19468. doi:10.1038/srep19468. [PubMed: 26782020]

[24]. Hutmacher DW, Scaffolds in tissue engineering bone and cartilage, Biomaterials 21 (2000) 2529–2543. doi:10.1016/S0142-9612(00)00121-6. [PubMed: 11071603]

[25]. Bose S, Roy M, Bandyopadhyay A, Recent advances in bone tissue engineering scaffolds, Trends Biotechnol 30 (2012) 546–554. doi:10.1016/j.tibtech.2012.07.005. [PubMed: 22939815]

[26]. Mistry AS, Mikos AG, Tissue Engineering Strategies for Bone Regeneration, in: Yannas IV (Ed.), Regen. Med. II Clin. Preclin. Appl, Springer Berlin Heidelberg, Berlin, Heidelberg, 2005: pp. 1–22. doi:10.1007/b99997.

[27]. Lee P, Tran K, Chang W, Fang Y-L, Zhou G, Junka R, Shelke NB, Yu X, Kumbar SG, Bioactive polymeric scaffolds for osteochondral tissue engineering: in vitro evaluation of the effect of culture media on bone marrow stromal cells, Polym. Adv. Technol 26 (2015) 1476–1485. doi: 10.1002/pat.3680.

[28]. Shanjani Y, Pan CC, Elomaa L, Yang Y, A novel bioprinting method and system for forming hybrid tissue engineering constructs, Biofabrication 7 (2015) 045008. doi: 10.1088/1758-5090/7/4/045008. [PubMed: 26685102]

[29]. Di Luca A, Ostrowska B, Lorenzo-Moldero I, Lepedda A, Swieszkowski W, Van Blitterswijk C, Moroni L, Gradients in pore size enhance the osteogenic differentiation of human mesenchymal stromal cells in three-dimensional scaffolds, Sci. Rep 6 (2016) 22898. doi:10.1038/srep22898. [PubMed: 26961859]

[30]. Ergun A, Yu X, Valdevit A, Ritter A, Kalyon DM, Radially and Axially Graded Multizonal Bone Graft Substitutes Targeting Critical-Sized Bone Defects from Polycaprolactone/Hydroxyapatite/ Tricalcium Phosphate, Tissue Eng. Part A 18 (2012) 2426–2436. doi:10.1089/ten.tea.2011.0625. [PubMed: 22764839]

[31]. Bracaglia LG, Smith BT, Watson E, Arumugasaamy N, Mikos AG, Fisher JP, 3D printing for the design and fabrication of polymer-based gradient scaffolds, Acta Biomater 56 (2017) 3–13. doi: 10.1016/j.actbio.2017.03.030. [PubMed: 28342878]

[32]. Bittner SM, Guo JL, Melchiorri A, Mikos AG, Three-dimensional printing of multilayered tissue engineering scaffolds, Mater. Today 21 (2018) 861–874. doi:10.1016/j.mattod.2018.02.006.

[33]. Sears NA, Seshadri DR, Dhavalikar PS, Cosgriff-Hernandez E, A Review of Three-Dimensional Printing in Tissue Engineering, Tissue Eng. Part B Rev 22 (2016) 298–310. doi:10.1089/ten.teb. 2015.0464. [PubMed: 26857350]

[34]. Gao G, Cui X, Three-dimensional bioprinting in tissue engineering and regenerative medicine, Biotechnol. Lett 38 (2016) 203–211. doi:10.1007/s10529-015-1975-1. [PubMed: 26466597]

[35]. Kundu J, Shim J-H, Jang J, Kim S-W, Cho D-W, An additive manufacturing-based PCL–alginate–chondrocyte bioprinted scaffold for cartilage tissue engineering, J. Tissue Eng. Regen. Med 9 (2015) 1286–1297. doi:10.1002/term.1682. [PubMed: 23349081]

[36]. Dababneh AB, Ozbolat IT, Bioprinting Technology: A Current State-of-the-Art Review, J. Manuf. Sci. Eng 136 (2014) 061016–061016–11. doi:10.1115/1.4028512.

[37]. Mohamed OA, Masood SH, Bhowmik JL, Optimization of fused deposition modeling process parameters: a review of current research and future prospects, Adv. Manuf 3 (2015) 42–53. doi: 10.1007/s40436-014-0097-7.

[38]. Murphy SV, Atala A, 3D bioprinting of tissues and organs, Nat. Biotechnol 32 (2014) 773–785. doi:10.1038/nbt.2958. [PubMed: 25093879]

[39]. Seol Y-J, Kang H-W, Lee SJ, Atala A, Yoo JJ, Bioprinting technology and its applications, Eur. J. Cardiothorac. Surg 46 (2014) 342–348. doi:10.1093/ejcts/ezu148. [PubMed: 25061217]

[40]. Zein I, Hutmacher DW, Tan KC, Teoh SH, Fused deposition modeling of novel scaffold architectures for tissue engineering applications, Biomaterials 23 (2002) 1169–1185. doi:10.1016/S0142-9612(01)00232-0. [PubMed: 11791921]

[41]. Bajaj P, Schweller RM, Khademhosseini A, West JL, Bashir R, 3D Biofabrication Strategies for Tissue Engineering and Regenerative Medicine, Annu. Rev. Biomed. Eng 16 (2014) 247–276. doi:10.1146/annurev-bioeng-071813-105155. [PubMed: 24905875]

[42]. Malik HH, Darwood ARJ, Shaunak S, Kulatilake P, El-Hilly AA, Mulki O, Baskaradas A, Three-dimensional printing in surgery: a review of current surgical applications, J. Surg. Res 199 (2015) 512–522. doi:10.1016/j.jss.2015.06.051. [PubMed: 26255224]

[43]. Trachtenberg JE, Placone JK, Smith BT, Piard CM, Santoro M, Scott DW, Fisher JP, Mikos AG, Extrusion-Based 3D Printing of Poly(propylene fumarate) in a Full-Factorial Design, ACS Biomater. Sci. Eng 2 (2016) 1771–1780. doi:10.1021/acsbiomaterials.6b00026.

[44]. Trachtenberg JE, Santoro M, Williams C, Piard CM, Smith BT, Placone JK, Menegaz BA, Molina ER, Lamhamedi-Cherradi S-E, Ludwig JA, Sikavitsas VI, Fisher JP, Mikos AG, Effects of Shear Stress Gradients on Ewing Sarcoma Cells Using 3D Printed Scaffolds and Flow Perfusion, ACS Biomater. Sci. Eng (2017). doi:10.1021/acsbiomaterials.6b00641.

[45]. Trachtenberg JE, Placone JK, Smith BT, Fisher JP, Mikos AG, Extrusion-based 3D printing of poly(propylene fumarate) scaffolds with hydroxyapatite gradients, J. Biomater. Sci. Polym. Ed 28 (2017) 532–554. doi:10.1080/09205063.2017.1286184. [PubMed: 28125380]

[46]. Gao G, Cui X, Three-dimensional bioprinting in tissue engineering and regenerative medicine, Biotechnol. Lett 38 (2016) 203–211. doi:10.1007/s10529-015-1975-1. [PubMed: 26466597]

[47]. Yin R, Zhang N, Wang K, Long H, Xing T, Nie J, Zhang H, Zhang W, Material design and photo-regulated hydrolytic degradation behavior of tissue engineering scaffolds fabricated via 3D fiber deposition, J. Mater. Chem. B 5 (2017) 329–340. doi:10.1039/C6TB02884E.

[48]. Luca AD, Longoni A, Criscenti G, Lorenzo-Moldero I, Klein-Gunnewiek M, Vancso Julius, van Blitterswijk C, Mota C, Moroni L, Surface energy and stiffness discrete gradients in additive manufactured scaffolds for osteochondral regeneration, Biofabrication 8 (2016) 015014. doi:10.1088/1758-5090/8/1/015014. [PubMed: 26924824]

[49]. Cao T, Ho K-H, Teoh S-H, Scaffold Design and in Vitro Study of Osteochondral Coculture in a Three-Dimensional Porous Polycaprolactone Scaffold Fabricated by Fused Deposition Modeling, Tissue Eng 9 (2003) 103–112. doi:10.1089/10763270360697012.

[50]. Temple JP, Hutton DL, Hung BP, Huri PY, Cook CA, Kondragunta R, Jia X, Grayson WL, Engineering anatomically shaped vascularized bone grafts with hASCs and 3D-printed PCL scaffolds, J. Biomed. Mater. Res. - Part A 102 (2014) 4317–4325. doi:10.1002/jbm.a.35107.

[51]. Heymer A, Bradica G, Eulert J, Nöth U, Multiphasic collagen fibre–PLA composites seeded with human mesenchymal stem cells for osteochondral defect repair: an in vitro study, J. Tissue Eng. Regen. Med 3 (2009) 389–397. doi:10.1002/term.175. [PubMed: 19434664]

[52]. Williams JM, Adewunmi A, Schek RM, Flanagan CL, Krebsbach PH, Feinberg SE, Hollister SJ, Das S, Bone tissue engineering using polycaprolactone scaffolds fabricated via selective laser sintering, Biomaterials 26 (2005) 4817–4827. doi:10.1016/j.biomaterials.2004.11.057. [PubMed: 15763261]

[53]. Zhou WY, Lee SH, Wang M, Cheung WL, Ip WY, Selective laser sintering of porous tissue engineering scaffolds from poly(l-lactide)/carbonated hydroxyapatite nanocomposite microspheres, J. Mater. Sci. Mater. Med 19 (2008) 2535–2540. doi:10.1007/s10856-007-3089-3. [PubMed: 17619975]

[54]. Zopf DA, Hollister SJ, Nelson ME, Ohye RG, Green GE, Bioresorbable Airway Splint Created with a Three-Dimensional Printer, N. Engl. J. Med 368 (2013) 2043–2045. doi:10.1056/NEJMc1206319. [PubMed: 23697530]

[55]. Bergmann C, Lindner M, Zhang W, Koczur K, Kirsten A, Telle R, Fischer H, 3D printing of bone substitute implants using calcium phosphate and bioactive glasses, J. Eur. Ceram. Soc 30 (2010) 2563–2567. doi:10.1016/j.jeurceramsoc.2010.04.037.

[56]. Bergmann CJD, Odekerken JCE, Welting TJM, Jungwirth F, Devine D, Bouré L, Zeiter S, V. Rhijn LW, Telle R, Fischer H, Emans PJ, Calcium Phosphate Based Three-Dimensional Cold Plotted Bone Scaffolds for Critical Size Bone Defects, BioMed Res. Int (2014). doi: 10.1155/2014/852610.

[57]. Bose S, Vahabzadeh S, Bandyopadhyay A, Bone tissue engineering using 3D printing, Mater. Today 16 (2013) 496–504. doi:10.1016/j.mattod.2013.11.017.

[58]. Inzana JA, Olvera D, Fuller SM, Kelly JP, Graeve OA, Schwarz EM, Kates SL, Awad HA, 3D printing of composite calcium phosphate and collagen scaffolds for bone regeneration, Biomaterials 35 (2014) 4026–4034. doi:10.1016/j.biomaterials.2014.01.064. [PubMed: 24529628]

[59]. Klammert U, Gbureck U, Vorndran E, Rödiger J, Meyer-Marcotty P, Kübler AC, 3D powder printed calcium phosphate implants for reconstruction of cranial and maxillofacial defects, J. Cranio-Maxillofac. Surg 38 (2010) 565–570. doi:10.1016/j.jcms.2010.01.009.

[60]. Diaz-Gomez LA, Smith BT, Kontoyiannis PD, Bittner SM, Melchiorri AJ, Mikos AG, Multimaterial segmented fiber printing for gradient tissue engineering, Tissue Eng. Part C Methods 25 (2018) 12–24. doi:10.1089/ten.tec.2018.0307. [PubMed: 30421648]

[61]. Bittner SM, Guo JL, Mikos AG, Spatiotemporal control of growth factors in three-dimensional printed scaffolds, Bioprinting (2018) e00032. doi:10.1016/j.bprint.2018.e00032. [PubMed: 31106279]

[62]. Jiang J, Tang A, Ateshian GA, Guo XE, Hung CT, Lu HH, Bioactive stratified polymer ceramic-hydrogel scaffold for integrative osteochondral repair, Ann. Biomed. Eng 38 (2010) 2183–2196. doi:10.1007/s10439-010-0038-y. [PubMed: 20411332]

[63]. Lewandrowski K-U, Bondre SP, Wise DL, Trantolo DJ, Enhanced bioactivity of a poly(propylene fumarate) bone graft substitute by augmentation with nano-hydroxyapatite, Biomed. Mater. Eng 13 (2003) 115–124. [PubMed: 12775902]

[64]. Liu Y, Lu Y, Tian X, Cui G, Zhao Y, Yang Q, Yu S, Xing G, Zhang B, Segmental bone regeneration using an rhBMP-2-loaded gelatin/nanohydroxyapatite/fibrin scaffold in a rabbit model., Biomaterials 30 (2009) 6276–6285. doi:10.1016/j.biomaterials.2009.08.003. [PubMed: 19683811]

[65]. Cunniffe GM, Curtin CM, Thompson EM, Dickson GR, O'Brien FJ, Content-Dependent Osteogenic Response of Nanohydroxyapatite: An in Vitro and in Vivo Assessment within Collagen-Based Scaffolds, ACS Appl. Mater. Interfaces 8 (2016) 23477–23488. doi:10.1021/acsami.6b06596. [PubMed: 27537605]

[66]. Sheikh Z, Sima C, Glogauer M, Bone Replacement Materials and Techniques Used for Achieving Vertical Alveolar Bone Augmentation, Materials 8 (2015) 2953–2993. doi:10.3390/ma8062953.

[67]. Catros S, Fricain J-C, Guillotin B, Pippenger B, Bareille R, Remy M, Lebraud E, Desbat B, Amédée J, Guillemot F, Laser-assisted bioprinting for creating on-demand patterns of human osteoprogenitor cells and nano-hydroxyapatite, Biofabrication 3 (2011) 025001. [PubMed: 21527813]

[68]. Guo T, Holzberg TR, Lim CG, Gao F, Gargava A, Trachtenberg JE, Mikos AG, Fisher JP, 3D printing PLGA: a quantitative examination of the effects of polymer composition and printing parameters on print resolution, Biofabrication 9 (2017) 024101. doi:10.1088/1758-5090/aa6370. [PubMed: 28244880]

[69]. Shim J-H, Yoon M-C, Jeong C-M, Jang J, Jeong S-I, Cho D-W, Huh J-B, Efficacy of rhBMP-2 loaded PCL/PLGA/β-TCP guided bone regeneration membrane fabricated by 3D printing technology for reconstruction of calvaria defects in rabbit, Biomed. Mater 9 (2014) 065006. [PubMed: 25384105]

[70]. ASTM D695–15, Standard Test Method for Compressive Properties of Rigid Plastics, ASTM International, West Conshohocken, PA, 2015.

[71]. Gibson LJ, Ashby MF, Cellular Solids: Structure and Properties 2nd ed., Cambridge: Cambridge University Press, 1997.

[72]. Gibson LJ, Harley BA, Ashby MF, Cellular materials in nature and medicine, Cambridge: Cambridge University Press, 2010.

[73]. Blaker JJ, Maquet V, Jérôme R, Boccaccini AR, Nazhat SN, Mechanical properties of highly porous PDLLA/Bioglass® composite foams as scaffolds for bone tissue engineering, Acta Biomater 1 (2005) 643–652. doi:10.1016/j.actbio.2005.07.003. [PubMed: 16701845]

[74]. Pabst W, Gregorová E, Tichá G, Elasticity of porous ceramics—A critical study of modulus −porosity relations, J. Eur. Ceram. Soc 26 (2006) 1085–1097. doi:10.1016/j.jeurceramsoc.2005.01.041.

[75]. Al-Ketan O, Rowshan R, Abu Al-Rub RK, Topology-mechanical property relationship of 3D printed strut, skeletal, and sheet based periodic metallic cellular materials, Addit. Manuf 19 (2018) 167–183. doi:10.1016/j.addma.2017.12.006.

[76]. Bajaj P, Schweller RM, Khademhosseini A, West JL, Bashir R, 3D Biofabrication Strategies for Tissue Engineering and Regenerative Medicine, Annu. Rev. Biomed. Eng 16 (2014) 247–276. doi:10.1146/annurev-bioeng-071813-105155. [PubMed: 24905875]

[77]. Lee J-S, Cha HD, Shim J-H, Jung JW, Kim JY, Cho D-W, Effect of pore architecture and stacking direction on mechanical properties of solid freeform fabrication-based scaffold for bone tissue engineering, J. Biomed. Mater. Res. A 100A (2012) 1846–1853. doi:10.1002/jbm.a.34149.

[78]. Shor L, Güçeri S, Wen X, Gandhi M, Sun W, Fabrication of three-dimensional polycaprolactone/hydroxyapatite tissue scaffolds and osteoblast-scaffold interactions in vitro, Biomaterials 28 (2007) 5291–5297. doi:10.1016/j.biomaterials.2007.08.018. [PubMed: 17884162]

[79]. Ragaert K, Cardon L, Baere ID, Degrieck J, Bulk mechanical properties of thermoplastic poly-ε-caprolactone, (n.d.) 5.

[80]. Heo S-J, Kim S-E, Wei J, Hyun Y-T, Yun H-S, Kim D-H, Shin JW, Shin J-W, Fabrication and characterization of novel nano- and micro-HA/PCL composite scaffolds using a modified rapid prototyping process, J. Biomed. Mater. Res. A 89A (2009) 108–116. doi:10.1002/jbm.a.31726.

[81]. Huang B, Caetano G, Vyas C, Blaker JJ, Diver C, Bártolo P, Polymer-Ceramic Composite Scaffolds: The Effect of Hydroxyapatite and β-tri-Calcium Phosphate, Materials 11 (2018) 129. doi:10.3390/ma11010129.

[82]. Kim JY, Lee T-J, Cho D-W, Kim B-S, Solid Free-Form Fabrication-Based PCL/HA Scaffolds Fabricated with a Multi-head Deposition System for Bone Tissue Engineering, J. Biomater. Sci. Polym. Ed 21 (2010) 951–962. doi:10.1163/156856209X458380. [PubMed: 20482995]

[83]. Kim MH, Yun C, Chalisserry EP, Lee YW, Kang HW, Park S-H, Jung W-K, Oh J, Nam SY, Quantitative analysis of the role of nanohydroxyapatite (nHA) on 3D-printed PCL/nHA composite scaffolds, Mater. Lett 220 (2018) 112–115. doi:10.1016/j.matlet.2018.03.025.

[84]. Wang H, Domingos M, Scenini F, Advanced mechanical and thermal characterization of 3D bioextruded poly(e-caprolactone)-based composites, Rapid Prototyp. J 24 (2018) 731–738. doi:10.1108/RPJ-10-2016-0165.

[85]. Gonçalves EM, Oliveira FJ, Silva RF, Neto MA, Fernandes MH, Amaral M, Vallet-Regí M, Vila M, Three-dimensional printed PCL-hydroxyapatite scaffolds filled with CNTs for bone cell growth stimulation, J. Biomed. Mater. Res. B Appl. Biomater 104 (2016) 1210–1219. doi:10.1002/jbm.b.33432. [PubMed: 26089195]

[86]. Nyberg E, Rindone A, Dorafshar A, Grayson WL, Comparison of 3D-Printed Poly-ε-Caprolactone Scaffolds Functionalized with Tricalcium Phosphate, Hydroxyapatite, Bio-Oss, or Decellularized Bone Matrix, Tissue Eng. Part A 23 (2016) 503–514. doi:10.1089/ten.tea.2016.0418.

[87]. Turnbull G, Clarke J, Picard F, Riches P, Jia L, Han F, Li B, Shu W, 3D bioactive composite scaffolds for bone tissue engineering, Bioact. Mater 3 (2018) 278–314. doi:10.1016/j.bioactmat.2017.10.001. [PubMed: 29744467]

[88]. Fu S-Y, Feng X-Q, Lauke B, Mai Y-W, Effects of particle size, particle/matrix interface adhesion and particle loading on mechanical properties of particulate–polymer composites, Compos. Part B Eng 39 (2008) 933–961. doi:10.1016/j.compositesb.2008.01.002.

[89]. Choi D, Marra KG, Kumta PN, Chemical synthesis of hydroxyapatite/poly(ε-caprolactone) composites, Mater. Res. Bull 39 (2004) 417–432. doi:10.1016/j.materresbull.2003.10.013.

[90]. Shim J-H, Jang K-M, Hahn SK, Park JY, Jung H, Oh K, Park KM, Yeom J, Park SH, Kim SW, Wang JH, Kim K, Cho D-W, Three-dimensional bioprinting of multilayered constructs containing human mesenchymal stromal cells for osteochondral tissue regeneration in the rabbit

knee joint, Biofabrication 8 (2016) 014102. doi:10.1088/1758-5090/8/1/014102. [PubMed: 26844597]

[91]. Zhang W, Lian Q, Li D, Wang K, Hao D, Bian W, He J, Jin Z, Cartilage Repair and Subchondral Bone Migration Using 3D Printing Osteochondral Composites: A One-Year-Period Study in Rabbit Trochlea, BioMed Res. Int 2014 (2014) e746138. doi:10.1155/2014/746138.

[92]. Shim J-H, Lee J-S, Kim JY, Cho D-W, Bioprinting of a mechanically enhanced three-dimensional dual cell-laden construct for osteochondral tissue engineering using a multi-head tissue/organ building system, J. Micromechanics Microengineering 22 (2012) 085014. doi: 10.1088/0960-1317/22/8/085014.

[93]. Trachtenberg JE, Placone JK, Smith BT, Piard CM, Santoro M, Scott DW, Fisher JP, Mikos AG, Extrusion-Based 3D Printing of Poly(propylene fumarate) in a Full-Factorial Design, ACS Biomater. Sci. Eng 2 (2016) 1771–1780. doi:10.1021/acsbiomaterials.6b00026.

[94]. Du Y, Liu H, Yang Q, Wang S, Wang J, Ma J, Noh I, Mikos AG, Zhang S, Selective laser sintering scaffold with hierarchical architecture and gradient composition for osteochondral repair in rabbits, Biomaterials 137 (2017) 37–48. doi:10.1016/j.biomaterials.2017.05.021. [PubMed: 28528301]

[95]. Moroni L, de Wijn JR, van Blitterswijk CA, 3D fiber-deposited scaffolds for tissue engineering: Influence of pores geometry and architecture on dynamic mechanical properties, Biomaterials 27 (2006) 974–985. doi:10.1016/j.biomaterials.2005.07.023. [PubMed: 16055183]

[96]. Van Bael S, Chai YC, Truscello S, Moesen M, Kerckhofs G, Van Oosterwyck H, Kruth J-P, Schrooten J, The effect of pore geometry on the in vitro biological behavior of human periosteum-derived cells seeded on selective laser-melted Ti6Al4V bone scaffolds, Acta Biomater 8 (2012) 2824–2834. doi:10.1016/j.actbio.2012.04.001. [PubMed: 22487930]

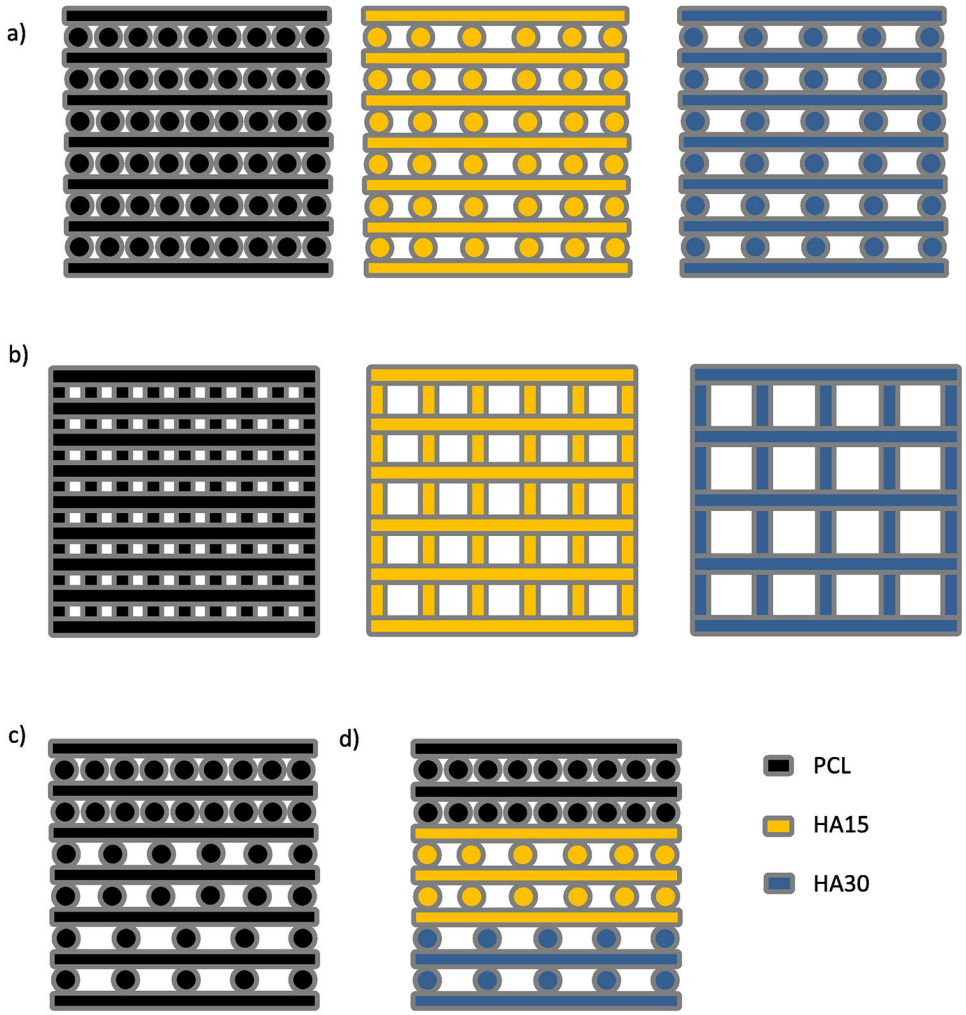

Fig. 1.

Three-dimensional printing schematic for the fabrication of PCL and PCL-HA constructs. (a) Side view of (L->R) Single-material, uniform porosity PCL (small-pore); HA15 (medium-pore); and HA30 (large-pore) scaffold design; (b) Top view of above scaffolds (c) (L->R) single-material, gradient porosity PCL scaffold, (d) multimaterial, gradient porosity scaffold.

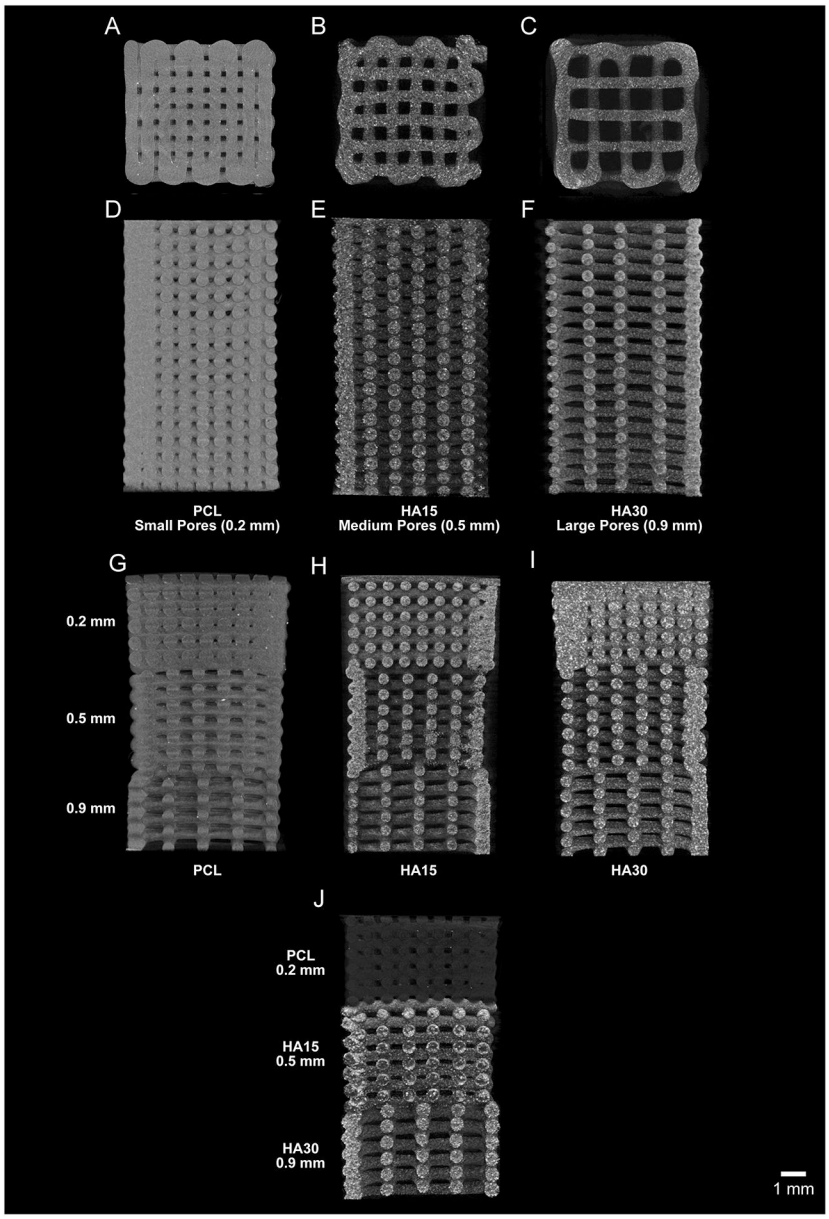

Fig. 2.

Representative micro-CT images of all uniform and gradient scaffolds included in the study (Table 1). Top-down and side views of PCL-only (small-pore; A, D), HA15 (mediumpore; B, E), and HA30 (large-pore; C, F) scaffolds respectively. Side view of gradient porosity PCL-only (G), HA15 (H), HA30 (I) scaffolds and Dual Gradient scaffold (J), respectively. Scale bar = 1 mm for all scaffold images.

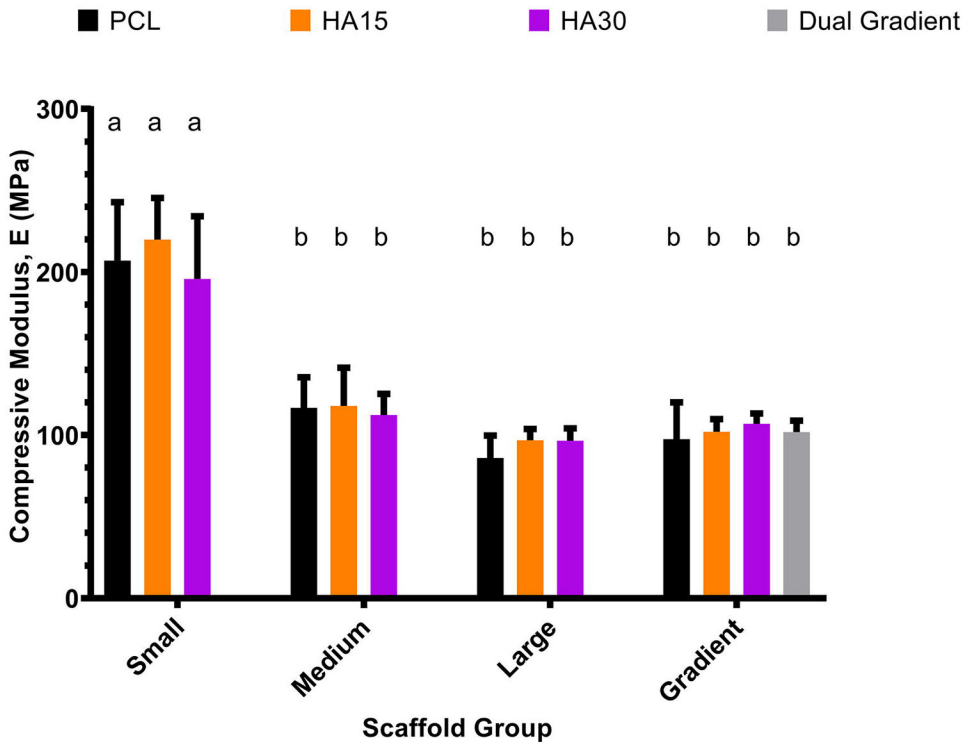

Fig. 3.

Compressive modulus as a function of pore morphology for all compositions examined (PCL-only, HA15, HA30, Dual gradient). Small-pore (0.2 mm) scaffolds demonstrated significantly higher compressive moduli than all other groups, while medium-pore (0.5 mm) and large-pore (0.9 mm) scaffolds were statistically similar. Moduli for single and dual gradient scaffolds were also similar to the medium and large pore scaffolds. Groups with the same letter are not statistically different ($p > 0.05$). $n = 5$ scaffolds for all groups.

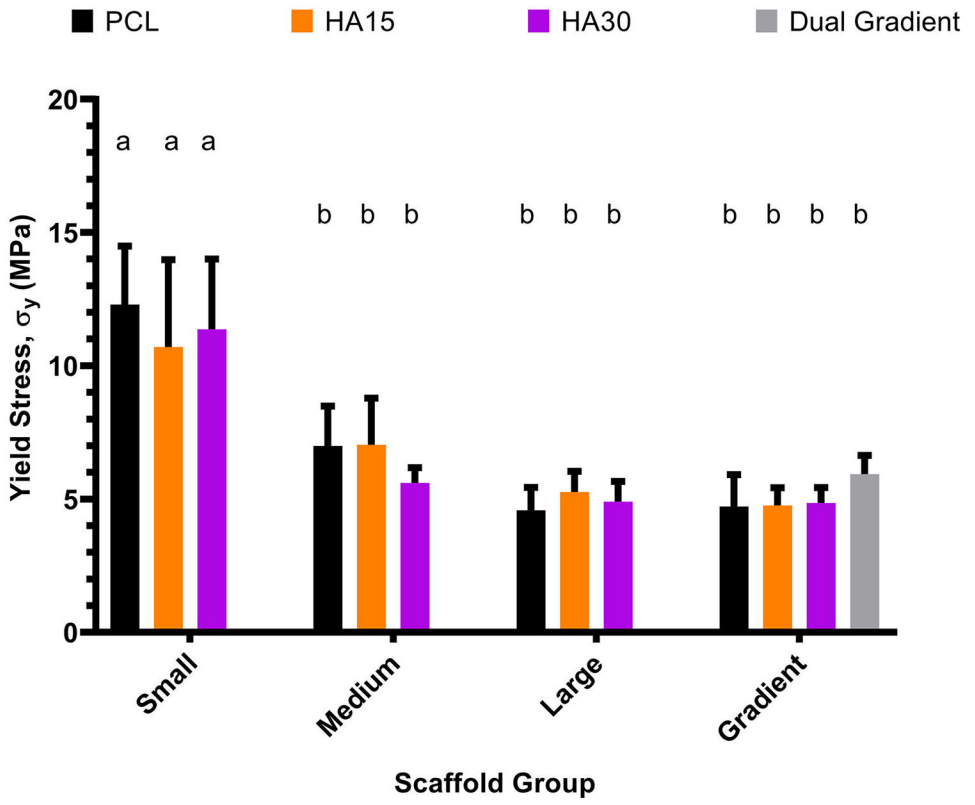

Fig. 4.

Yield stress as a function of pore morphology for all compositions examined (PCLonly, HA15, HA30, Dual Gradient). Similar to the results for compressive modulus, small-pore scaffolds had higher yield stresses compared to all other groups, which were statistically similar ($p < 0.05$). Groups with the same letter are not statistically different ($p > 0.05$). $n = 5$ scaffolds for all groups.

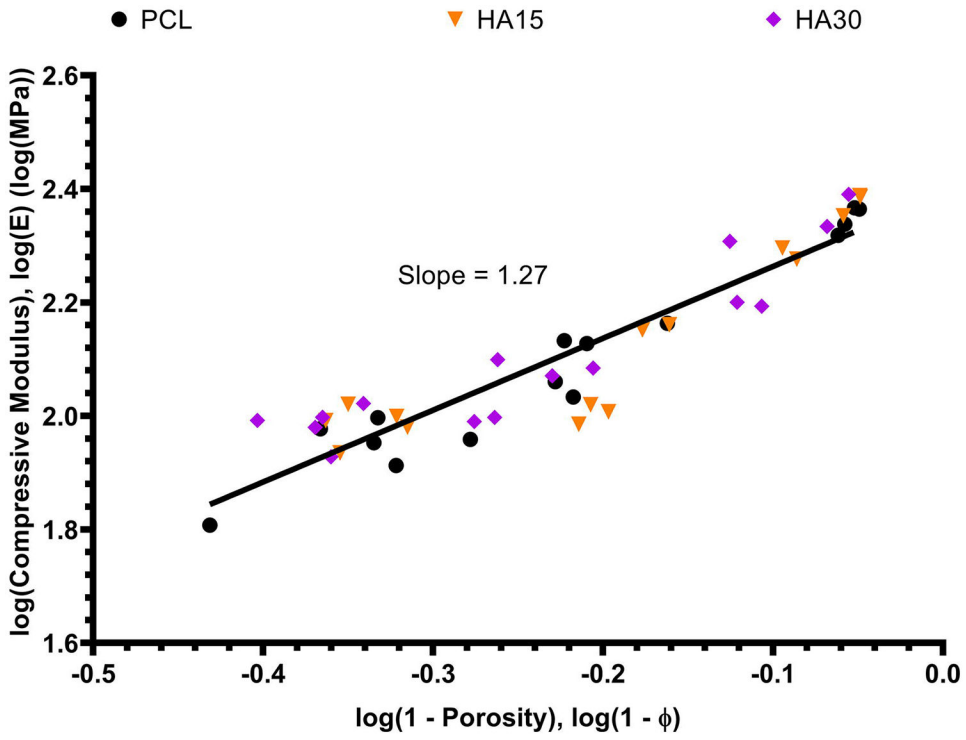

Fig. 5.

Compressive modulus as a continuous function of pre-compression porosity for all uniform (0.2 mm, 0.5 mm, 0.9 mm) scaffolds of each composition. The model equation describing these data was determined to be $\log(E) = 1.27\log(1 - \varphi) + 2.39$ with $R^2 = 0.8698$.

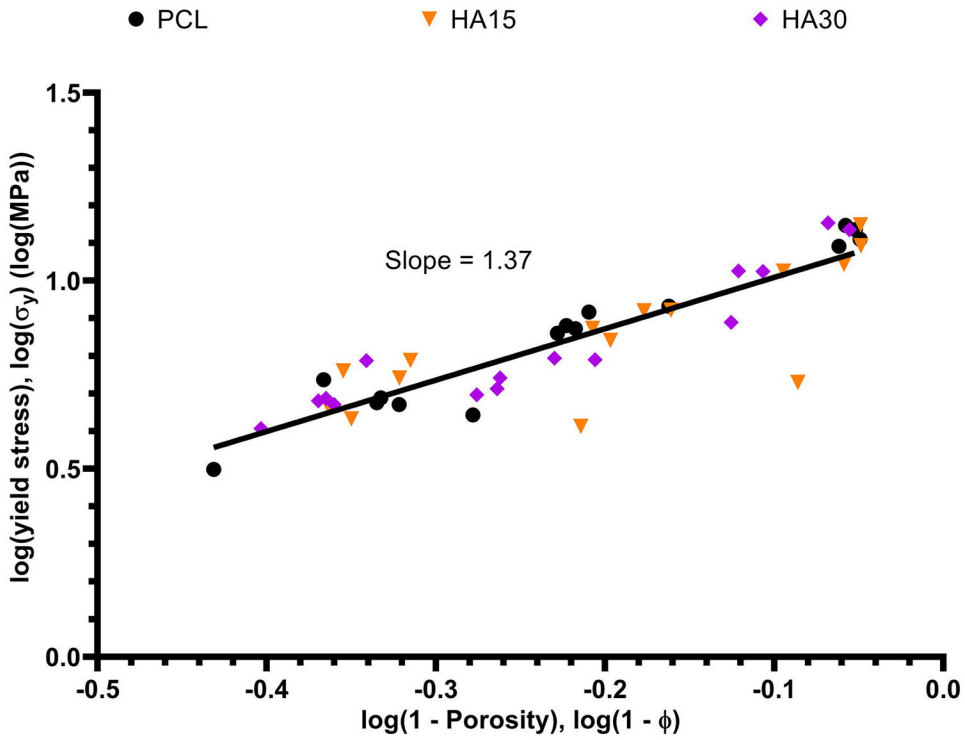

Fig. 6.

Yield stress as a continuous function of pre-compression porosity for all uniform (0.2 mm, 0.5 mm, 0.9 mm) scaffolds of each composition. The model equation describing these data was determined to be $\log(E) = 1.37\log(1 - \varphi) + 1.15$ with $R^2 = 0.8057$.

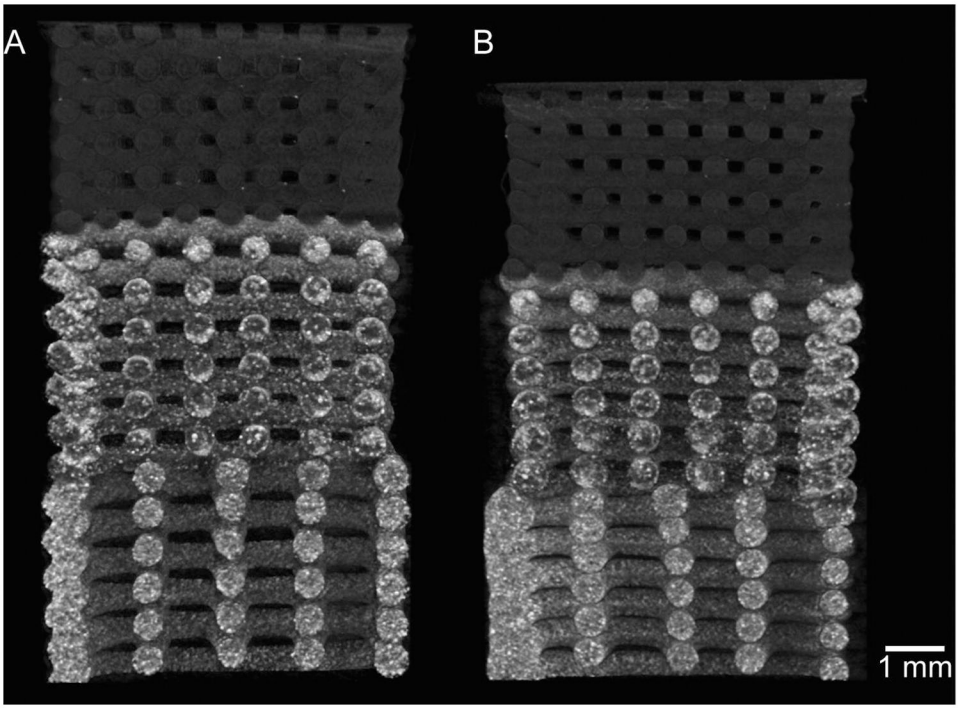

Fig. 7.

Representative micro-CT images of dual gradient scaffold as described in Table 1 (top section - PCL/0.2 mm pores, middle section - HA15/0.5 mm pores, bottom section - HA30/0.9 mm pores) A) before and B) after compression to 20% strain and subsequent recovery. Scale bar = 1 mm.

Table 1:

List of scaffold groups

Scaffold Group	Material	Pore Size Pattern
PCL - Small	PCL (uniform)	Small – 0.2 mm (uniform)
PCL - Medium	PCL (uniform)	Medium – 0.5 mm (uniform)
PCL - Large	PCL (uniform)	Large – 0.9 mm (uniform)
PCL - Gradient	PCL (uniform)	Small – 0.2 mm (top section) Medium – 0.5 mm (middle section) Large – 0.9 mm (bottom section)
HA15 - Small	85 wt% PCL, 15 wt% HA (uniform)	Small – 0.2 mm (uniform)
HA15 - Medium	85 wt% PCL, 15 wt% HA (uniform)	Medium – 0.5 mm (uniform)
HA15 - Large	85 wt% PCL, 15 wt% HA (uniform)	Large – 0.9 mm (uniform)
HA15 - Gradient	85 wt% PCL, 15 wt% HA (uniform)	Small – 0.2 mm (top section) Medium – 0.5 mm (middle section) Large – 0.9 mm (bottom section)
HA30 - Small	70 wt% PCL, 30 wt% HA (uniform)	Small – 0.2 mm (uniform)
HA30 - Medium	70 wt% PCL, 30 wt% HA (uniform)	Medium – 0.5 mm (uniform)
HA30 - Large	70 wt% PCL, 30 wt% HA (uniform)	Large – 0.9 mm (uniform)
HA30 - Gradient	70 wt% PCL, 30 wt% HA (uniform)	Small – 0.2 mm (top section) Medium – 0.5 mm (middle section) Large – 0.9 mm (bottom section)
Dual Gradient	PCL (top section) 85 wt% PCL, 15 wt% HA (middle section) 70 wt% PCL, 30 wt% HA (bottom section)	Small – 0.2 mm (top section) Medium – 0.5 mm (middle section) Large – 0.9 mm (bottom section)

Table 2:

List of scaffold printing conditions/parameters

Material	Temperature (°C)	Pressure (bar)	Speed (mm/s)	Pre-Flow (s)	Post-Flow (s)	Wait Time (s)
PCL	160	5.0	1.2	0.5	0.25	0
HA15	160	5.0	0.9	0.7	0.75	35
HA30	160	5.5	0.8	0.7	0.75	30